Photo-Scanning Electrochemical Microscopy Observation of Overall Water Splitting at a Single Aluminum-Doped Strontium Titanium Oxide Microcrystal

Gaukhar Askarova,[†,§] *Chengcan Xiao,*[‡] *Koushik Barman,*[†] *Xiang Wang,*[†,§] *Lihua Zhang,*[%] *Frank E. Osterloh,*[‡,*] *and Michael V. Mirkin*[†,#,*]

[†] Department of Chemistry and Biochemistry, Queens College, Flushing, NY 11367, USA

[§] The Graduate Center of CUNY, New York, NY 10016

[‡] Department of Chemistry, University of California Davis, Davis, CA, 95616.

[#] Advanced Science Research Center at The Graduate Center, CUNY; New York, NY 10031

[%] Center for Functional Nanomaterials, Brookhaven National Laboratory, Upton, NY 11973.

e-mail: fosterloh@ucdavis.edu; mmirkin@qc.cuny.edu

ABSTRACT

Particulate photocatalysts for the overall water-splitting (OWS) reaction offer promise as devices for hydrogen fuel generation. Even though such photocatalysts have been studied for nearly five decades, much of the understanding of their function is derived from observations of catalyst ensembles and macroscopic photoelectrodes. This is because the sub-micrometer size of most OWS photocatalysts makes spatially resolved measurements of their local reactivity very difficult. Here we employ photo-scanning electrochemical microscopy (photo-SECM) to quantitatively measure hydrogen and oxygen evolution at individual OWS photocatalyst particles for the first time. Micrometer-sized Al-doped $SrTiO_3/Rh_{2-y}Cr_yO_3$ photocatalyst particles were immobilized on a glass substrate and interrogated with a chemically modified SECM nanotip. The tip simultaneously served as a light guide to illuminate the photocatalyst and as an electrochemical nanoprobe to observe oxygen and hydrogen fluxes from OWS. Local O_2 and H_2 fluxes obtained from chopped light experiments and photo-SECM approach curves using a

COMSOL Multiphysics finite-element model confirmed stoichiometric H_2/O_2 evolution of 9.3/4.6 μmol cm^{-2} h^{-1} with no observable lag during chopped illumination cycles. Additionally, photoelectrochemical experiments on a single microcrystal attached to a nanoelectrode tip revealed a strong light intensity dependence of the OWS reaction. These results provide the first confirmation of OWS at single micrometer-sized photocatalyst particles. The developed experimental approach is an important step towards assessing the activity of photocatalyst particles at the nanometer scale.

INTRODUCTION

The photocatalytic overall water-splitting (OWS) process represents a promising technology for sustainable hydrogen fuel generation from water.[1,2] Particle-based photocatalysts for the reaction essentially are miniature photoelectrochemical devices that achieve simultaneous water reduction and oxidation under excitation with light. Because oxygen evolution and hydrogen evolution sites are only separated by nanometers (compared to centimeters in ordinary photoelectrochemical cells), pH gradients between the anodic and cathodic regions can be minimized. This reduces energy loss from pH-related electrochemical overpotentials [3,4] and allows electrolysis of pure water without added electrolytes. However, generating electrochemical potential differences in excess of 1.5 V to drive OWS on the microscale is no easy task; it requires both long-lived charge carriers and efficient mechanisms to separate them. Furthermore, OWS catalysts must be able to suppress the thermodynamically favorable oxygen reduction reaction, which reduces the efficiency of fuel-formation.[5] This can be achieved by making the hydrogen evolution cocatalyst selective for proton reduction.[6] Because of these attributes, OWS photocatalysts must be viewed as a separate technology from solar fuel photoelectrodes, which only drive one electrochemical reaction, not two.[7,8]

Even though OWS photocatalysts have been around for over 40 years,[9] no experiment has observed oxygen and hydrogen evolution processes at individual catalyst particles during operation (in operando). Instead, most of our understanding of the working principles of OWS catalysts is based on electrochemical studies of macroscopic photoelectrodes,[9b] H_2/O_2 evolution experiments on particle suspensions,[10] electrochemical measurements of catalyst ensembles,[11] photolabeling reactions,[12] and theoretical modeling.[13] However, in-operando observations on individual photocatalyst particles are now within reach, as sub-micrometer resolution is achievable with several techniques, including single-molecule fluorescence microscopy,[14] transient absorption microscopy,[15] surface photovoltage kelvin probe force microscopy (SPV-KFM),[16] scanning electrochemical cell microscopy,[17] potential-sensing atomic force microscopy,[18] and scanning electrochemical microscopy (SECM).[19,20] A suitable target for such studies is the Al-doped $SrTiO_3/Rh_{2-y}Cr_yO_3$ OWS photocatalyst. This catalyst employs Al-doped $SrTiO_3$ nanoparticles as water oxidation photoanode and $Rh_{2-y}Cr_yO_3$ as selective proton reduction electrocatalysts. Thin films of the material use sunlight to generate hydrogen with a solar to hydrogen efficiency of 0.76%,[21,22] and optimized versions drive OWS with unity quantum efficiency under 350-360 nm illumination.[23] Although this material is the most advanced OWS photocatalyst today, questions remain about its inner workings. For example, while photolabeling studies suggest that charge separation is controlled by the electron accepting and hole accepting properties of the {100} and {110} facets on $SrTiO_3$,[23] electrochemical measurements combined with modeling conclude that charge separation in the system is controlled mainly by the local kinetics of the O_2/H_2O and H_2O/H_2 redox reactions.[24] Measurements on individual particles would bring insight into this problem, but to-date microscopic level observations of the $SrTiO_3/Rh_{2-y}Cr_yO_3$ catalyst are rare, and have not yet

achieved sufficient resolution.

In SECM, the reactivity of electrocatalysts is probed by scanning a small tip electrode above the catalyst's surface to measure local reactant and product fluxes and determine the local rates of specific heterogeneous reactions. Micrometer-sized SECM probes have been extensively used in studies of photoelectrochemical processes [25-31] and for screening of photoelectrochemical and photocatalytic properties of different materials.[32-34] Simpson and Rodríguez-López used smaller (240 nm radius) tips for redox nanotitrations by surface interrogation SECM to characterize reactivity of adsorbed intermediates on pristine and ion-milled defective areas of n-doped (100) $SrTiO_3$ photoelectrodes.[35] They measured bimolecular rates of the reaction between the titrant and adsorbate and reported dramatic differences in these rate constants, suggesting that modifications made to the surface influence the reactivity of photogenerated reactive oxygen species. Abruña and co-workers [36] used SECM in combination with operando-X-ray reflectivity to investigate the changes in structure and reactivity of a $SrTiO_3$ layer upon application of an external bias. In addition to probing the photogenerated O_2, they performed SECM to evaluate surface coverage with a reactive OH ad-layer.

The tips employed in all SECM experiments mentioned above were too large to provide nanoscale spatial resolution required for single particle experiments and active site mapping. For example, Onishi and coworkers used a 10 μm microelectrode as an SECM tip to determine the absolute O_2 evolution rate on the photocatalyst film cast on a glass plate.[37a] They simulated oxygen diffusion to fit experimental photoelectrochemical transients and evaluate the oxygen evolution reaction (OER) rate. O_2 evolution was found to lag tens of seconds behind light excitation which was attributed to the filling of trap states by the initially generated charge carriers. When excitation stopped, the O_2 evolution rate decayed exponentially in seconds.[37a] In

a follow-up study,[37b] the team used a similar approach on Al-doped $SrTiO_3$ /RhCrOx / CoOy to observe instantaneous O_2 adsorption and desorption in addition to steady, photocatalytic O_2 evolution under intense light irradiation. They speculated that O_2 adsorption likely involved binding and oxidation of surface Ti^{3+} sites near the oxygen vacancies, and O_2 desorption followed the reverse sequence.

Here we employ nm-sized SECM probes for the first in-operando observation of photoelectrochemical hydrogen and oxygen evolution from a single cubic $Rh_{2-y}Cr_yO_3$ decorated Al-doped $SrTiO_3$ microparticulate photocatalyst, designated as a 'cube' in the following. The tip simultaneously served as an electrochemical nanoprobe collecting oxygen and hydrogen fluxes produced by the photocatalytic reaction and as a light guide illuminating the cube surface.[31,38,39] The three types of SECM experiments used to image topography and to map surface reactivity of a single cube are shown schematically in Fig. 1. In the feedback mode experiment (Fig. 1A), the tip electrode is brought within a short distance from the cube immobilized on a glass surface. The electrolyte contains no redox mediator except for dissolved oxygen and the tip potential (E_T) is such that only the oxygen reduction reaction (ORR) occurs on its surface. When the separation distance between the tip and substrate (d) is small (i.e., comparable to tip radius, a), the i_T decreases with decreasing d because of the hindered diffusion of O_2 (negative feedback; the tip current near the surface is lower than its value in the bulk solution, i.e., $i_T < i_{T,\infty}$) due to the cube

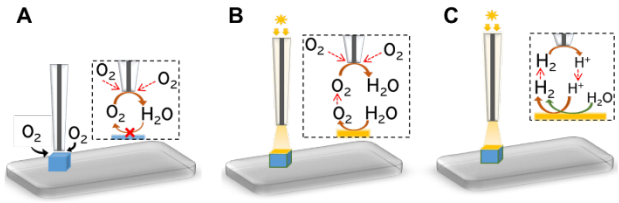

Figure 1. Schematic representation of photo-SECM experiments at a single Al:$SrTiO_3$/$Rh_xCr_yO_z$ cube. (A) Negative SECM feedback produced in the dark by the inert cube surface blocking O_2 diffusion to the tip. (B) SG/TC of photogenerated O_2. (C) SG/TC of photogenerated H_2 coupled

with the positive SECM feedback due to the H_2 oxidation at the tip and proton reduction at the cube surface. Not to scale.

acting as a physical barrier; no oxygen generation occurs on the cube in the dark.

In the substrate generation/tip collection (SG/TC) mode of photo-SECM, the tip is biased at a suitable potential (E_T) to collect a product (either H_2 or O_2) of water splitting on the catalyst surface under illumination. At a negative E_T, oxygen generated on the microcrystal surface is reduced at the tip electrode (Fig. 1B). At a positive E_T, the tip collects H_2 produced by water reduction on the cube surface (Fig. 1C). The hydrogen oxidation reaction (HOR) occurring at the tip produces protons that diffuse to the cube surface and get reduced back to H_2. This process results in the positive SECM feedback shown in Fig. 1C. The tip current (i_T) can be recorded either as a function of d (approach curve) or tip x–y position (imaging). Since the diffusion-limited current density at a nm-sized electrode is very high, an inner-sphere electron transfer (ET) process (e.g., ORR or HOR) occurring at a nanotip typically produces a kinetic current at any attainable overpotential. Although the electrocatalytic mechanism is complicated and not completely known, the kinetic tip current density can be defined as:

$$j(r,z) = nFk_Tc(r,z) \quad (1)$$

where r and z are, respectively, the co-ordinates in the directions radial and normal to the tip surface, n is the number of transferred electrons (i.e., 4 for ORR and 2 for HOR at a Pt tip), F is the Faraday constant, k_T is the effective heterogeneous rate constant at a specific E_T value, and $c(r,z)$ is the local concentration or redox species at the tip surface. The theory for SG/TC mode of SECM with a kinetic tip current was developed recently.[40]

The currents produced by inner-sphere ET processes, including HOR and ORR at metal (e.g., Pt) nanoelectrodes are typically unstable and not suitable for SECM imaging

experiments.[41] Reagents, products, and intermediates can passivate the electrode surface, and adsorbed impurities block active atoms needed to carry out such a reaction.[42,43] The smaller the tip electrode the stronger the effects of its surface deactivation or contamination, and the harder to measure signals produced by HOR and ORR. This problem has recently been overcome by chemically modifying the surface of a carbon or Pt nanotip with redox species to enable mediated ET between the nanoelectrode surface and dissolved H_2 or O_2.[41] Nanoelectrodes modified with $Ru(bpy)_3$ complex or ferrocene (Fc) molecules have been used to measure a broad range of oxidation and reduction processes, including ORR, HOR.[41] Here we employ Fc-modified Pt nanoprobes in conjunction with through-tip illumination to investigate water-splitting processes at single Al:$SrTiO_3$ cubes. Additionally, we demonstrate the possibility of photo-electrochemical experiments at a single microcrystal attached to a nanoelectrode tip.

EXPERIMENTAL SECTION

Chemicals. Titanium(IV) oxide (P25) (99.5%, Acros Organics), strontium carbonate (99.9%, Sigma Aldrich), strontium chloride hexahydrate (99%, EM Science), rhodium chloride (>99%), chromium(III) nitrate nonahydrate (99%, Acros Organics), alumina crucibles (Fisherbrand, 99.7% alumina) and acetone (for HPLC, ⩾99.9%, Sigma Aldrich), potassium sulfate (99% Sigma Aldrich), (6-bromohexyl)ferrocene (Sigma Aldrich), tetrabutylammonium tetrafluoroborate ($TBABF_4$, 99%, Sigma Aldrich), and acetonitrile (⩾99.9%, Sigma Aldrich) were used as received. Water used for synthesis was purified to 17.5 MΩ cm resistivity by a Nano-pure system. Aqueous solutions for SECM experiments were prepared using deionized water from the Milli-Q Advantage A10 system equipped with Q-Gard T2 Pak, a Quantum TEX cartridge, and a VOC pak; total organic carbon (TOC) <3 ppb.

Synthesis. Al-doped strontium titanate (Al:$SrTiO_3$) particles were synthesized using the published procedure[44] by conducting a solid state synthesis followed by flux treatment. 1.68 g TiO_2 and 3.10 g $SrCO_3$ were ground with a mortar and pestle. The resulting powder was transferred into a covered ceramic crucible and annealed at 1000 ℃ for 10 hours, followed by natural cool down to room temperature. This yields non-doped $SrTiO_3$ powder in 93% yield. 0.3 g of the powder was then mixed with 4.371 g $SrCl_2{\cdot}6H_2O$ ground together using a mortar and pestle. The mixture was then transferred to an open alumina crucible and annealed at 1100 ℃ for 10 h in air, followed by slow cooling to 600 ℃ by 1 ℃/min and then by natural cooling to room temperature. The grey molten solid was washed with water until no white AgCl precipitate formed in the supernatant upon adding a dilute aqueous $AgNO_3$ solution. Then, the solid was dried at 70 ℃ in an oven overnight to yield 83% of Al-doped $SrTiO_3$ crystals.

Ultrasonication was employed to obtain micrometer-sized cubes from the flux-mediated Al:$SrTiO_3$ sample. 40 mg flux-mediated Al:$SrTiO_3$ powder was dispersed in 4 mL water via ultrasonication for 2 h. The suspension was then kept for 2 min allowing sedimentation of large aggregates. Then the supernatant was transferred to another vial, and large particles were allowed to sediment for 2 h, after which the supernatant was removed and disposed. Next, the precipitate in the vial was washed 5 times with water to remove Al:$SrTiO_3$ nanoparticles. For a typical washing cycle, water was added to the precipitate to reach the same volume as before, followed by a 5 min ultrasonication and 1 h sedimentation, after which the supernatant was discarded. This was repeated 4 times, after which the precipitate was dried in an oven at 70 ℃ overnight to yield the product in 7% yield.

$Rh_xCr_{2-x}O_3$ cocatalyst was loaded onto the surface of Al:$SrTiO_3$ particles using the published procedure[44] with a weight ratio of Rh:Cr:$SrTiO_3$:Al = 1:1:1000. Typically, 150 mg

Al:$SrTiO_3$ was mixed with 1.5 mL of 0.972 mmol/L $RhCl_3$ solution (containing 0.1 mg Rh/mL) and 1.5 mL of 1.92 mmol/L $Cr(NO_3)_3$ solution (containing 0.1 mg Cr/mL) in a vial in a 70 ℃ water bath, and water was slowly evaporated under constant stirring. The product was then transferred to a furnace and heated at 350 ℃ in air for 1 h to produce $Rh_xCr_{2-x}O_3$-loaded Al:$SrTiO_3$ in 95% yield.

$Rh_xCr_{2-x}O_3$-loaded Al:$SrTiO_3$ particle films were made on sodium borate glass by dispersing 1 mg of Al:$Rh_xCr_{2-x}O_3$/$SrTiO_3$ in 15 mL water via 15 min sonication to form a uniform suspension. 200 μL of the suspension was drop-coated on the surface of a 40 mm glass petri dish, dried overnight, then annealed at 350 ℃ for 1 h in air in a box furnace with a ramping rate of 10 ℃/min. The particle film was then naturally cooled to room temperature and used for electrochemical experiments. The details of Al:$Rh_xCr_{2-x}O_3$/$SrTiO_3$ characterization are available in the Supporting Information (Figures S4-S6).

Fabrication of Pt nanoelectrodes. Disk-type Pt nanoelectrodes were fabricated by pulling 25 μm-diameter annealed Pt wires (Goodfellow) into borosilicate capillaries (Drummond; O D, 1.0 mm; ID, 0.2 mm) with the help of a P-2000 laser puller (Sutter Instrument Co.).[45] The pulled tips were polished on a 50 nm alumina disk (Precision Surfaces International) under video microscopic control and sonicated in deionized water for 10 s. A microforge (model MF-900, Narishige, Tokyo, Japan) was used to reduce the RG (i.e., the ratio of glass radius to that of the conductive tip) of the tapered tip. The appropriate protection was used to avoid electrostatic damage to the nanoelectrodes.[46] The tip size and shape were evaluated from TEM images (Fig. S2) and SECM approach curves.[47]

Modification of Pt nanoelectrodes. Ferrocene was attached to the Pt nanoelectrode surface using an earlier reported procedure for the reduction of primary monohaloalkanes.[48] A Pt

nanoelectrode was biased a negative potential (-2.0 V *vs.* $Ag/AgNO_3$) for 20 seconds in acetonitrile solution of 5 mM (6-bromohexyl)ferrocene containing 0.1 M $TBABF_4$ under an inert atmosphere. The modified electrodes were washed carefully with acetonitrile and water. The same Fc modified tip was used to measure O_2 and H_2 fluxes. While ORR occurred at the Pt surface, and its current was not greatly affected by chemical modification, HOR was mediated by the surface-bound Fc molecules.[41]

SECM setup and procedures. SECM experiments were carried out using a previously described home-built instrument.[49] The 3-electrode arrangement was employed with MSE (Hg/Hg_2SO_4) and Pt wire serving as a reference and a counter electrode, respectively. All experiments were performed in a glass petri dish (BR455701, MilliporeSigma). The nanoelectrode tip was initially positioned a few tens of micrometers above a single $SrTiO_3$ cube with the help of a long-distance video microscope. A digital angle gauge (DWL-80Pro, Digi-Pas) was used to ensure the horizontal orientation of the substrate plane and the correct tip/substrate alignment. A current *vs*. distance curve was obtained during the subsequent fine approach. All experiments were carried out in a Faraday cage at room temperature (23 ± 2 ºC). The current offset of the potentiostat (~2 pA) was subtracted from all measured current values.

For photo-electrochemical experiments, the SECM instrument was coupled with the optical setup similar to that described previously.[39b] Briefly, the optical setup (Newport Corporation) consisted of an OPS-A500 500 W power supply, a 250 W HgXe lamp with a fiber bundle focusing assembly (model 77776) attached to its housing (model 67005), and broad wavelength range optical fiber (model 78277, UV-VIS Single Fiber Cable) with a core diameter 1 mm. An IR cutoff FSQ-KG3 glass filter (Newport) was used to minimize sample heating during the experiment. The optical fiber was coupled with an SECM tip using a complex lens system.[39b]

The light from the fiber was focused on the back of the tip, while the glass sheath of the nanoelectrode acted as a light-guide focalizing the radiation on the substrate area facing the tip. All experiments (except for Figure 8) were conducted with light source power fixed at 250 W. A PM100D power and energy meter (Thorlabs) with a silicon photodiode power sensor (S130VC) was used to detect the output power through optical fiber and custom focusing optics. Unlike previously reported bulk experiments,[50] no oxygen or hydrogen bubble formation was detected in SECM experiments.

Finite-element simulations. Simulations were carried out using COMSOL Multiphysics version 5.6 commercial package. Axisymmetric 2D models were built to simulate the SECM experiments, including negative feedback and SG/TC modes. The "transport of dilute species" model was used to solve the steady-state diffusion problems. The COMSOL modeling reports are available in the Supporting Information.

RESULTS AND DISCUSSION

Topography imaging of $SrTiO_3$ cubes by SECM with O_2 mediator. The ORR based negative feedback was employed to locate and image a single Al:$SrTiO_3$ $Rh_xCr_yO_z$ cube in the dark (Fig. 2). The data reveals that the cube has ~2 µm edge length (Fig. 2A) and contains a smaller cube on top of it, as seen also in the corresponding optical image (Fig. 2B). The presence of the smaller cube necessitated a relatively large vertical distance between the tip and the top facet of the main cube, which, consequently, produced only a blurred image. Higher

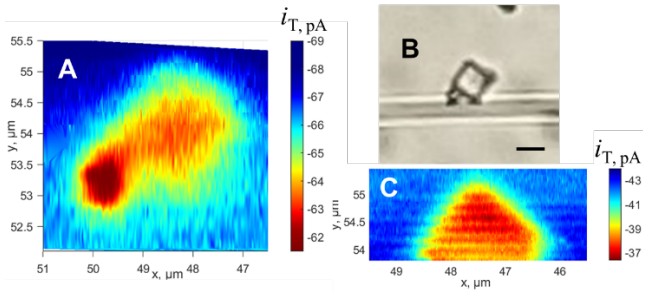

Figure 2. 2D SECM topography image of the Al:$SrTiO_3$ $Rh_xCr_yO_z$ cube attached to the glass surface (A), optical micrograph of the same cube (B), and a more detailed image of a portion of the same cube scanned at a closer separation distance (C). Solution contained 0.1 M K_2SO_4, a = 180 nm, E_T , V = -1.1 (A) and -0.95 (C) *vs*. Hg/Hg_2SO_4. Scale bar in B is 2 μm.

spatial resolution (Fig. 2C) was achieved when a portion of the top facet of the same cube was imaged with a much smaller d. The small variation of the current across the surface shows that (100) facet has no surface irregularities, but the cube is apparently positioned at a slight angle on the glass substrate (with its top corner in the image elevated towards the probe).

Evaluating OER rate at the Al:$SrTiO_3$ $Rh_xCr_yO_z$ cube by SG/TC mode of SECM.

Two current-distance curves (Fig. 3A; symbols) were obtained with the same SECM tip approaching the top facet of the cube imaged in Fig. 2. An oxygen reduction current at the tip was observed in the dark (Fig. 3A, curve 1) and under illumination (Fig. 3A, curve 2) at E_T = -0.95 V *vs.* Hg/Hg_2SO_4. To evaluate the tip/cube separation distance, d, curve 1 was fitted to the theory for the ORR-based negative feedback (solid green line[40]). At any given d, the difference between the current values measured under illumination (curve 2) and in the dark (curve 1) represents the flux of oxygen photogenerated at the cube surface and collected at the tip (*cf.* Figs 1B and 1A). The f_{O_2} = 1.3 nmol cm^{-2} s^{-1} value was obtained from the fit of the experimental approach curve (red symbols in Fig. 3A) to the theory (green solid curve[40]), and the corresponding current density of water oxidation, assuming $4e^-$ OER, is 0.50 mA/cm^2.

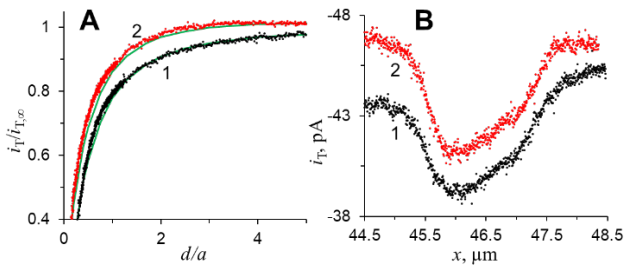

Figure 3. Experimental (symbols) and theoretical (solid lines) approach curves (A) and lateral scans (B) obtained with the same Fc-modified Pt tip over the same spot on the top face of the Al:$SrTiO_3$ $Rh_xCr_yO_z$ crystal in the dark (1) and under illumination (2). Both theoretical curves were calculated for a = 180 nm and RG = 8. The tip current is due to ORR in 0.1 M K_2SO_4 solution (pH 7). E_T = -0.95 V *vs.* Hg/Hg_2SO_4. k_T = 0.79 cm/s.

The flux of photogenerated oxygen collected at the tip can also be evaluated from lateral scans recorded by moving the tip in the horizontal plane across the top facet of the same cube in the dark (Fig. 3B, curve 1) and under illumination (curve 2). When the tip was scanned above the top facet of the cube, it was closer to the sample surface than during the scan above the underlying glass, and i_T was lower in agreement with the approach curves in Fig. 3A. The shapes of the two line scans are similar, reflecting a slightly slanted top face of the cube, as mentioned above. The light-induced difference between the currents is ~2 pA over the entire portion of the line scan over the cube surface. According to curve 1 in Fig. 3A, i_T = 39 pA (black curve in Fig. 3B) corresponds to d = 142 nm. The corresponding current value under illumination (~42 pA in Fig. 3B, red curve) is very close to the i_T value corresponding d = 142 nm under illumination (i.e., 43 pA in Fig. 3A curve 2). Thus, similar ORR flux values can be extracted from SECM lateral line scans and approach curves.

A more convenient way to evaluate the photogenerated flux of O_2 is by analyzing chopped light tip current transients (Fig. 4A). A sequence of 10 s long transients was recorded at the Pt tip positioned over the top face of an Al:$SrTiO_3$ $Rh_xCr_yO_z$ cube (both the cube and the tip are the same as those in Fig. 3). The separation distance (d = 20 nm) was evaluated from the steady-state tip current measured in the dark (~10 pA in Fig. 4A) using the theoretical approach curve (curve 1 in Fig. 3A). The amplitude of the photocurrent transient (Δi_T = 6.8 pA in Fig. 4A) is equivalent to the difference between the tip currents measured under illumination and in the dark

for the same d. To determine the oxygen flux, one can use f_{O_2} as a fitting parameter and calculate the theoretical Δi_T *vs.* d curve corresponding to d and Δi_T values found from the photocurrent transients. The Δi_T - d curve in Fig. 4B was calculated for f_{O_2} = 1.3 nmol cm^{-2} s^{-1} and k_T = 0.79 cm/s by subtracting curve 1 from curve 2 in Fig. 3A. The inset in Fig. 8B shows a close-up of the short-distance part of this curve, and the red dot corresponds to Δi_T = 6.8 pA and d = 20 nm. Since the experimental point obtained from Fig. 8A lies exactly on the Δi_T - d curve derived from Fig. 3A, the oxygen flux value extracted from photocurrent transients is the same as that found by fitting approach curves to the theory (i.e., f_{O_2} = 1.3 nmol cm^{-2} s^{-1}). Although the analysis of chopped light photocurrent transients is equivalent to that of current–distance curves, measuring Δi_T is more straightforward and accurate. An advantage of this approach is that the current transients can be measured at a very short separation distance, thus increasing the flux of photogenerated oxygen to the tip.

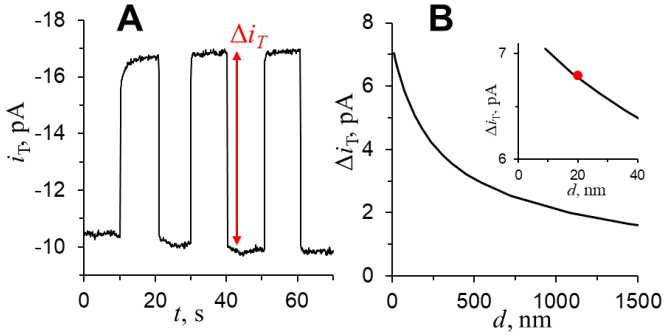

Figure 4. (A) Chopped light current transients for ORR at the tip positioned over the same spot on the top face of the Al:$SrTiO_3$ $Rh_xCr_yO_z$ cube as in Fig. 3A. The tip is the same as in Fig. 3. E_T = -0.95 V *vs.* Hg/Hg_2SO_4. (B) Δi_T *vs.* d curve obtained by subtracting the i_T values simulated for the same d with (curve 2 in Fig. 3A) and without (curve 1 in Fig. 3A) illumination. Inset: magnified portion of the Δi_T-d curve (Fig. 4B). The red circle represents the amplitude of the photocurrent transient (Δi_T = 6.8 pA) recorded at d = 20 nm (panel A).

The i_T transients in Fig. 4A are very fast with the rise time in the range of milliseconds. By contrast, the current transients at a micrometer-sized electrode positioned above a $SrTiO_3$

photocatalyst film doped with Al were markedly slower with the rise time in the range of tens of seconds.[37] Our data suggests that the slow response observed in ref. 37 is likely due to mass-transport and illumination issues and not a result of the intrinsic OER mechanism of the individual photocatalyst particles.

Evaluating hydrogen evolution rate at the Al:$SrTiO_3$ $Rh_xCr_yO_z$ cube by SG/TC mode of SECM. Unlike ORR discussed above, HOR at a Fc-modified nanotip is a mediated ET process. The density of Fc molecules immobilized on the Pt surface is significantly lower than on porous carbon tips,[41] resulting in relatively small k_T values and low kinetic tip currents. Thus, reliable measurement of the photogenerated H_2 flux is only possible at short separation distances ($d/a < 1$), where the tip current is amplified by positive feedback produced by the reduction of protons on the sample surface (see the inset in Fig. 1C). When the tip is far from the cube, the proton reduction current is negligible because of the low concentration of protons in the pH 7 solution. However, at short separation distances the tip generates a high flux of protons that diffuse to the top face of the cube and get photo-reduced at the small portion of its surface facing the tip.

To probe hydrogen evolution reaction (HER) at the cube, an experimental approach curve (Fig. 5, symbols) was obtained using the same tip over the same location on the $SrTiO_3$ surface as in Figs. 3 and 4 but with E_T = 0.4 V *vs.* Hg/Hg_2SO_4 suitable for HOR. The distance scale was established according to curve 1 in Fig. 3A. The experimental $i_T - d$ curve was fitted to the SG/TC of hydrogen theory (solid line in Fig. 5; one should notice that physical rather than normalized variables are used here, unlike Fig. 3A, because $i_{T,\infty}$= 0 for HOR). The kinetic tip current was calculated from Eq. (1) with independently measured k_T = 0.14 cm/s (for details, see Supporting Information). The tip parameters used for the fit (i.e., a = 180 nm and RG = 8) were

the same as in Fig. 3A. Importantly, the flux of hydrogen generated by water reduction at the cube surface, f_{H2} = 2.6 nmol cm^{-2} s^{-1} extracted from the fit is exactly twice that of the water oxidation (1.3 nmol cm^{-2} s^{-1}). Therefore, the current density of water reduction (0.50 mA/cm^2) equals that determined for the water oxidation. This value translates into H_2/O_2 evolution rates of 9.3/4.6 μmol cm^{-2} h^{-1}which is about half of what was observed for a $SrTiO_3/RhCrO_x$ film under UV illumination from a 300 W Xe lamp (20/10 μmol cm^{-2} h^{-1}).[22] However, a direct comparison is difficult due to the unknown light intensity at the end of the SCEM tip.

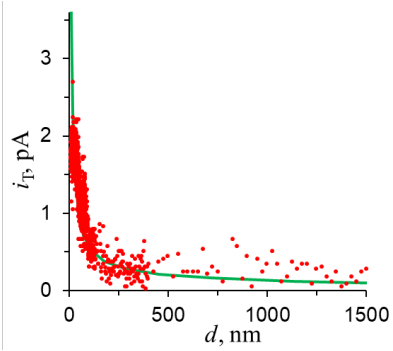

Figure 5. Experimental approach curve (symbols) obtained under illumination with a Fc-modified Pt tip approaching the same spot on the surface of the Al:$SrTiO_3$ $Rh_xCr_yO_z$ crystal as in Fig. 3A and fitted to the theory (solid line) for SG/TC of hydrogen. The tip was the same as in Figs. 3 and 4. The tip current was due to HOR in 0.1 M K_2SO_4 solution (pH 7). E_T = 0.4 V *vs.* Hg/Hg_2SO_4. The theoretical curve was calculated for a = 180 nm and RG = 8. k_T = 0.14 cm/s. The approach velocity was decreased at $d \approx$ 400 nm.

The analysis of photocurrent transients for HER/HOR (Fig. 6A) is similar to that discussed above for water oxidation, except that the tip current in the dark is negligibly low, and no subtraction is required to construct the theoretical distance dependence of the photogenerated

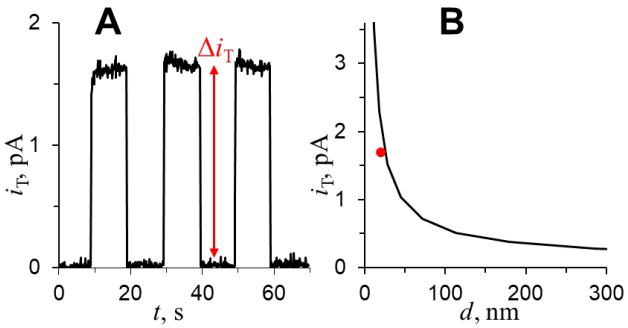

Figure 6. (A) Chopped light current transients for HOR at the same tip position as in Fig. 4A. E_T = 0.4 V *vs.* Hg/Hg_2SO_4. (B) The magnified short-distance portion of the theoretical approach curve (Fig. 5, solid line). The red circle represents the amplitude of the photocurrent transient recorded at d = 20 nm (panel A).

hydrogen oxidation current at the tip (Fig. 6B). The transients in Fig. 6A were recorded at the same tip position as in Fig. 4A, and the experimental point (red circle in Fig. 6B) extracted from Fig. 6A for d = 20 nm is very close to the simulated i_T-d curve.

Photoelectrochemical experiments at an Al:$SrTiO_3$ $Rh_xCr_yO_z$ cube attached to an SECM tip. An alternative approach to probing photoelectrochemistry at a single microcrystal is by attaching it to the SECM tip. An approach curve (Fig. 7A) was obtained by bringing the tip vertically toward the illuminated surface of an Al:$SrTiO_3$ $Rh_xCr_yO_z$ cube. As expected, the hydrogen collection current at the tip (E_T = 0.4 V *vs.* Hg/Hg_2SO_4) increased when it was moved toward the cube surface. However, this approach curve is only qualitatively similar to that in Fig. 5, and it could not be quantitatively fit to the theory. The likely reason is that the conductive disk of this tip was slightly recessed, and i_T increased when its insulating sheath pushed against the cube surface. The maximum current in Fig. 7A (~10 pA) is significantly larger than the i_T values in Figs. 5 and 6, suggesting that at the point of the closest approach the distance between the conductive disk and the cube was only a few nm.

Unexpectedly, when the tip was retracted from the glass surface containing the $SrTiO_3$ photocatalyst particles, the current value, $i_T \approx 10$ pA, remained essentially constant over the tip displacement of ~800 nm (Fig. 7B), indicating that the actual distance between the Pt disk and the cube did not change. The current, however, dropped to near-zero after the light was switched off and the cube stopped generating H_2 (the inset in Fig. 7B). These findings suggest that the cube was attached to the glass shroud of the SECM tip, which was confirmed by optical micrographs (Figs. 7C,D).

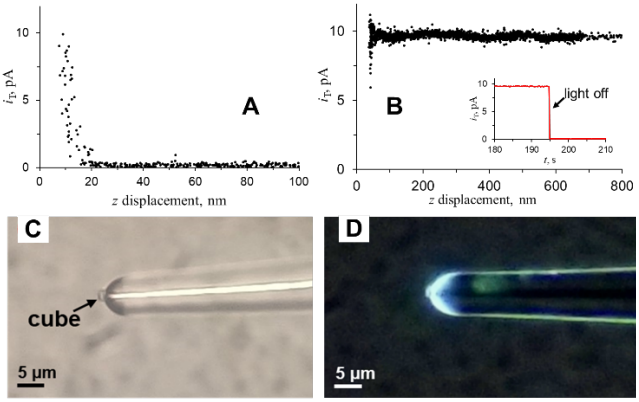

Figure 7. "Fishing" for a $SrTiO_3$ cube with an SECM tip. (A) Current *vs.* tip displacement curve based on hydrogen oxidation at the Fc-modified Pt tip approaching the cube in 0.1 M K_2SO_4 solution under through-tip illumination. (B) The retraction curve obtained by reversing the tip motion after reaching the point of the closest approach in (A). The inset: the abrupt current drop caused by switching off the light after the tip was moved back ~800 nm. $a \approx 160$ nm; $E_T = 0.4$ V *vs.* Hg/Hg_2SO_4. Optical micrographs of the Al:$SrTiO_3$ $Rh_xCr_yO_z$ cube attached to the Pt tip (C) in the dark and (D) under through-tip illumination.

The high stability of this fixed arrangement enables OWS experiments at small and constant separation distance. Chopped light measurements with the cube attached to the tip are shown in Fig. S3A. The current rises and decays instantaneously on the time scale of the experiment. Qualitatively, this response is similar to those measured by in SECM experiments without attachment. Variable light intensity-chopped-light current transients of HOR are shown

in Fig. 8A. As expected, the HOR and OER photocurrents increase with light intensity. A plot of the HOR photocurrent amplitude versus the electric power of the light source (Fig. 8B) shows a linear trend, as expected for a photocatalyst with constant quantum efficiency.[51] This confirms that the immobilized cube retains most of its photocatalytic activity despite the proximity to the SECM tip.

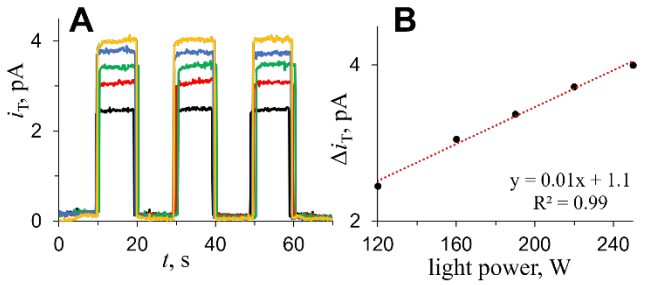

Figure 8. (A) Chopped-light current transients of HOR obtained with a $SrTiO_3$ cube attached to the Pt tip at different light intensities. From top to bottom, the light source power was: 250, 220, 190, 160, and 120 W. (B) The amplitude of the photocurrent transient *vs.* light source power. E_T = 0.4 V *vs.* Hg/Hg_2SO_4. Solution contained 0.1 M K_2SO_4.

CONCLUSIONS

In summary, we described the first observation of OWS at a single photocatalyst particle. Measurements were conducted using the substrate generation/tip collection (SG/TC) mode of SECM on a micrometer sized Al:$SrTiO_3$ $Rh_xCr_yO_z$ photocatalyst particle immobilized on a glass support. Because overall water splitting at an unbiased microcrystal produces no net electric current, SECM is the only technique available for probing the intrinsic kinetics of both OER and HER. Detection of local H_2 and O_2 fluxes was achieved during approach curves, lateral line scans, and photocurrent transients. In order to quantitatively analyze the kinetic tip currents, a finite-element model was developed for SG/TC and feedback modes of SECM that allowed quantification of O_2 and H_2 fluxes with the same microcrystal and the same SECM tip. A current density of 0.50 mA/cm^2 was observed for HER and OER, corresponding to H_2/O_2 evolution rates

of 9.3/4.6 μmol cm^{-2} h^{-1}, as expected for overall water splitting. Furthermore, HER and OER experiments with an immobilized photocatalyst reveal light intensity-dependent photocatalytic activity, in agreement with the theory. Lastly, it must be noted that the observed fluxes and photocurrent densities are average values for the top cube face because the 100-200 nm radius SECM tips employed in this study were too large for mapping the heterogeneous surface reactivity at higher resolution. Increased spatial resolution may be achievable in photo-SECM measurements with smaller (e.g., ~20 nm) chemically modified tips underway in our laboratories.

■ ASSOCIATED CONTENT

Supporting Information. Procedures for determination of k_T for ORR and HOR at a Fc-modified Pt tip, additional current-time recordings, a TEM image of an SECM tip, and chopped-light photocurrent transients, including Figures S1 – S6 and COMSOL simulation reports. This material is available free of charge via the Internet at http://pubs.acs.org.

■ AUTHOR INFORMATION

Author Contributions

All authors have given approval to the final version of the manuscript.

Notes

The authors declare no competing financial interest.

■ ACKNOWLEDGMENTS

The support of this work by the U.S. Department of Energy, Office of Basic Energy Sciences under Grant No. DE-SC0017603 (MVM) and DOE-SC0015329 (FEO) is gratefully acknowledged.

■ REFERENCES

1. Segev, G.; Kibsgaard, J.; Hahn, C.; Xu, Z.J.; Cheng, W.H.; Deutsch, T.G.; Xiang, C.; Zhang, J.Z.; Hammarström, L.; Nocera, D.G.; Weber, A.Z.; Agbo, P.; Hisatomi, T.; Osterloh, F.E.; Domen, K.; Abdi, F.F.; Haussener, S.; Miller, D.J.; Ardo, S.; McIntyre, P.C.; Hannappel, T.; Hu, S.; Atwater, H.; Gregoire, J.M.; Ertem, M.Z.; Sharp, I.D.; Choi, K.S.; Lee, J.S.; Ishitani, O.; Ager, J.W.; Prabhakar, R.R.; Bell, A.T.; Boettcher, S.W.; Vincent, K.; Takanabe, K.; Artero, V.; Napier, R.; Cuenya, B.R.; Koper, M.T.M.; Van De Krol, R.; Houle, F. The 2022 Solar Fuels Roadmap. *J. Phys. D: Appl. Phys* **2022**, *55*, 323003. DOI: 10.1088/1361-6463/ac6f97
2. Pinaud, B.A.; Benck, J.D.; Seitz, L.C.; Forman, A.J.; Chen, Z.B.; Deutsch, T.G.; James, B.D.; Baum, K.N.; Baum, G.N.; Ardo, S.; Wang, H.L.; Miller, E.; Jaramillo, T.F. Technical and Economic Feasibility of Centralized Facilities for Solar Hydrogen Production via Photocatalysis and Photoelectrochemistry. *Energ. Environ. Sci.* **2013**, *6*, 1983-2002. DOI: 10.1039/c3ee40831k
3. Qureshi, M.; Garcia-Esparza, A.T.; Shinagawa, T.; Sautet, P.; Le Bahers, T.; Takanabe, K. Contribution of Electrolyte in Nanoscale Electrolysis of Pure and Buffered Water by Particulate Photocatalysis. *Sustain. Energy Fuels* **2018**, *2*, 2044-2052. DOI: 10.1039/C8SE00272J
4. Jin, J.; Walczak, K.; Singh, M.R.; Karp, C.; Lewis, N.S.; Xiang, C. An Experimental and Modeling/Simulation-Based Evaluation of the Efficiency and Operational Performance Characteristics of an Integrated, Membrane-free, Neutral pH Solar-Driven Water-Splitting System. *Energy Environ. Sci.* **2014**, *7*, 3371-3380. DOI: 10.1039/C4EE01824A
5. Maeda, K.; Teramura, K.; Lu, D. L.; Saito, N.; Inoue, Y.; Domen, K. Noble-Metal/Cr_2O_3 Core/Shell Nanoparticles as a Cocatalyst for Photocatalytic Overall Water Splitting. *Angew. Chem., Int. Ed.* **2006**, *45*, 7806-7809. DOI: 10.1002/anie.200602473
6. Wang, Q.; Domen, K. Particulate Photocatalysts for Light-Driven Water Splitting: Mechanisms, Challenges, and Design Strategies. *Chem. Rev.* **2020**, *120*, 919-985. DOI: 10.1021/acs.chemrev.9b00201
7. Osterloh, F.E. Photocatalysis versus Photosynthesis: A Sensitivity Analysis of Devices for Solar Energy Conversion and Chemical Transformations. *ACS Energy Lett.* **2017**, *2*, 445-453. DOI: 10.1021/acsenergylett.6b00665
8. Nielander, A.C.; Shaner, M.R.; Papadantonakis, K.M.; Francis, S.A.; Lewis, N.S. A Taxonomy for Solar Fuels Generators. *Energ. Environ. Sci.* **2015**, *8*, 16-25. DOI: 10.1039/C4EE02251C
9. (a) Domen, K.; Naito, S.; Soma, M.; Onishi, T.; Tamaru, K. Photocatalytic Decomposition of Water-Vapor on an NiO-$SrTiO_3$ Catalyst. *J. Chem. Soc., Chem. commun.* **1980**, *12*, 543-544. DOI: 10.1039/C39800000543
   (b) Morrison, S.R. *Electrochemistry at semiconductor and oxidized metal electrodes*; Plenum Press: New York, 1980; p. 416.
10. Qureshi, M.; Takanabe, K. Insights on Measuring and Reporting Heterogeneous Photocatalysis: Efficiency Definitions and Setup Examples. *Chem. Mater.* **2017**, *29*, 158-167. DOI: 10.1021/acs.chemmater.6b02907
11. Minegishi, T.; Nishimura, N.; Kubota, J.; Domen, K. Photoelectrochemical Properties of $LaTiO_2N$ Electrodes Prepared by Particle Transfer for Sunlight-Driven Water Splitting. *Chem. Sci.* **2013**, *4*, 1120-1124. DOI: 10.1039/c2sc21845c

12. Kobayashi, T.; Taniguchi, Y.; Yoneyama, H.; Tamura, H. Effective Surfaces of Semiconductor Catalysts for Light-Induced Heterogeneous Reactions Evaluated by Simultaneous Photodeposition of both Oxidation and Reduction Products. *J. Phys. Chem.* **1983**, *87*, 768-775. DOI: 0.1021/j100228a015
13. Garcia-Esparza, A.T.; Takanabe, K. A Simplified Theoretical Guideline for Overall Water Splitting Using Photocatalyst Particles. *J. Mater. Chem. A* **2016**, *4*, 2894-2908. DOI: 10.1039/C5TA06983A
14. (a) Sambur, J. B.; Chen, T.-Y.; Choudhary, E.; Chen, G.; Nissen, E. J.; Thomas, E. M.; Zou, N.; Chen, P., Sub-Particle Reaction and Photocurrent Mapping to Optimize Catalyst-Modified Photoanodes. *Nature* **2016,** *530,* 77-80. DOI: 10.1038/nature16534
(b) Hesari, M.; Sambur, J. B.; Mao, X.; Jung, W.; Chen, P., Quantifying Photocurrent Loss of a Single Particle–Particle Interface in Nanostructured Photoelectrodes. *Nano Lett.* **2019,** *19,* 958-962. DOI: 10.1021/acs.nanolett.8b04188
(c) Mao, X.; Chen, P. Inter-Facet Junction Effects on Particulate Photoelectrodes. *Nat. Mater.* **2022**, *21*, 331-337. DOI: 10.1038/s41563-021-01161-6
15. Guo, Z.; Manser, J.S.; Wan, Y.; Kamat, P.V.; Huang, L. Spatial and Temporal Imaging of Long-Range Charge Transport in Perovskite Thin Films by Ultrafast Microscopy. *Nat. Commun.* **2015**, *6*, 7471. DOI: 10.1038/ncomms8471
16. (a) Chen, R.; Fan, F.; Dittrich, T.; Li, C. Imaging Photogenerated Charge Carriers on Surfaces and Interfaces of Photocatalysts with Surface Photovoltage Microscopy. *Chem. Soc. Rev*. **2018**, *47*, 8238-8262. DOI: 10.1039/C8CS00320C
(b) Shearer, M.J.; Li, M.-Y.; Li, L.-J.; Jin, S.; Hamers, R.J. Nanoscale Surface Photovoltage Mapping of 2D Materials and Heterostructures by Illuminated Kelvin Probe Force Microscopy. *J. Phys. Chem. C* **2018**, *122*, 13564-13571. DOI: 10.1021/acs.jpcc.7b12579
17. Choi, M.; Siepser, N. P.; Jeong, S.; Wang, Y.; Jagdale, G.; Ye, X.; Baker, L. A. Probing Single-Particle Electrocatalytic Activity at Facet-Controlled Gold Nanocrystals. *Nano Lett.* **2020**, *20*, 1233-1239. DOI: 10.1021/acs.nanolett.9b04640
18. (a) Nellist, M.R.; Laskowski, F.A.L.; Qiu, J.; Hajibabaei, H.; Sivula, K.; Hamann, T.W.; Boettcher, S.W. Potential-Sensing Electrochemical Atomic Force Microscopy for In Operando Analysis of Water-Splitting Catalysts and Interfaces. *Nat. Energy* **2018**, *3*, 46-52. DOI: 10.1038/s41560-017-0048-1
(b) Laskowski, F.A.L.; Oener, S.Z.; Nellist, M.R.; Gordon, A.M.; Bain, D.C.; Fehrs, J.L.; Boettcher, S.W. Nanoscale Semiconductor/Catalyst Interfaces in Photoelectrochemistry. *Nat. Mater*. **2020**, *19*, 69-76. DOI: 10.1038/s41563-019-0488-z
19. Wittstock, G.; Rastgar, S.; Scarabin, S. Local Studies of Photoelectrochemical Reactions at Nanostructured Oxides. *Curr. Opin. Electrochem.* **2019**, *13*, 25-32. DOI: 10.1016/j.coelec.2018.10.007
20. Hill, C. M.; Pan, S. SECM Techniques for Locally Interrogating the Photocatalytic Activity of Semiconducting Materials for Solar-Driven Chemical Transformations. In *Scanning Electrochemical Microscopy*, 3rd ed.; Bard, A. J.; Mirkin, M. V., Eds.; CRC Press: Boca Raton, 2022, pp. 361-378.
21. Nishiyama, H.; Yamada, T.; Nakabayashi, M.; Maehara, Y.; Yamaguchi, M.; Kuromiya, Y.; Nagatsuma, Y.; Tokudome, H.; Akiyama, S.; Watanabe, T.; Narushima, R.; Okunaka, S.; Shibata, N.; Takata, T.; Hisatomi, T.; Domen, K. Photocatalytic Solar Hydrogen Production from Water on a 100-m^2 Scale. *Nature* **2021**, *598*, 304-307. DOI: 10.1038/s41586-021-03907-3

22. Goto, Y.; Hisatomi, T.; Wang, Q.; Higashi, T.; Ishikiriyama, K.; Maeda, T.; Sakata, Y.; Okunaka, S.; Tokudome, H.; Katayama, M.; Akiyama, S.; Nishiyama, H.; Inoue, Y.; Takewaki, T.; Setoyama, T.; Minegishi, T.; Takata, T.; Yamada, T.; Domen, K. A Particulate Photocatalyst Water-Splitting Panel for Large-Scale Solar Hydrogen Generation. *Joule* **2018**, *2*, 509-520. DOI: 10.1016/j.joule.2017.12.009
23. Takata, T.; Jiang, J.; Sakata, Y.; Nakabayashi, M.; Shibata, N.; Nandal, V.; Seki, K.; Hisatomi, T.; Domen, K. Photocatalytic Water Splitting with a Quantum Efficiency of Almost Unity. *Nature* **2020**, *581*, 411-414. DOI: 10.1038/s41586-020-2278-9
24. Pan, Z.; Yanagi, R.; Wang, Q.; Shen, X.; Zhu, Q.; Xue, Y.; Röhr, J.A.; Hisatomi, T.; Domen, K.; Hu, S. Mutually-Dependent Kinetics and Energetics of Photocatalyst/Co-Catalyst/Two-Redox Liquid Junctions. *Energy Environ. Sci*. **2020**, *13*, 162-173. DOI: 10.1039/C9EE02910A.
25. Casillas, N.; James, P.; Smyrl, W. H. A Novel Approach to Combine Scanning Electrochemical Microscopy and Scanning Photoelectrochemical Microscopy. *J. Electrochem. Soc.* **1995,** *142,* L16-L18. DOI: 10.1149/1.2043970.
26. Haram, S. K.; Bard, A. J. Scanning Electrochemical Microscopy. 42. Studies of the Kinetics and Photoelectrochemistry of Thin Film CdS/Electrolyte Interfaces. *J. Phys. Chem. B* **2001**, *105*, 8192-8195. DOI: 10.1021/jp011068j
27. Harati, M.; Jia, J.; Giffard, K.; Pellarin, K.; Hewson, C.; Love, D. A.; Lau, W. M.; Ding, Z. One-Pot Electrodeposition, Characterization & Photoactivity of CIGS Thin Films for Solar Cells. *Phys. Chem. Chem. Phys.* **2010**, *12*, 15282-15290. DOI: 10.1039/c0cp00586j
28. Esposito, D. V.; Levin, I.; Moffat, T. P.; Talin, A. A. H_2 Evolution at Si-Based Metal-Insulator-Semiconductor Photoelectrodes Enhanced by Inversion Channel Charge Collection and H Spillover. *Nat. Mater.* **2013**, *12*, 562–568. DOI: 10.1038/nmat3626
29. Park, H.S.; Leonard, K.C.; Bard, A.J. Surface Interrogation Scanning Electrochemical Microscopy (SI-SECM) of Photoelectrochemistry at a W/Mo-$BiVO_4$ Semiconductor Electrode: Quantification of Hydroxyl Radicals during Water Oxidation. *J. Phys. Chem. C* **2013**, *117*, 12093-12102. DOI: 10.1021/jp400478z
30. Aaronson, B. D. B.; Byers, J. C.; Colburn, A. W.; McKelvey, K.; Unwin, P. R. Scanning Electrochemical Cell Microscopy Platform for Ultrasensitive Photoelectrochemical Imaging *Anal. Chem.* **2015**, *87*, 4129-4133. DOI: 10.1021/acs.analchem.5b00288
31. Conzuelo, F.; Sliozberg, K.; Gutkowski, R.; Grützke, S.; Nebel, M.; Schuhmann, W. High-Resolution Analysis of Photoanodes for Water Splitting by Means of Scanning Photoelectrochemical Microscopy. *Anal. Chem.* **2017**, *89*, 1222-1228. DOI: 10.1021/acs.analchem.6b03706
32. Lee, J. W.; Ye, H. C.; Pan, S. L.; Bard, A. J. Screening of Photocatalysts by Scanning Electrochemical Microscopy. *Anal. Chem.* **2008**, *80*, 7445-7450. DOI: 10.1021/ac801142g
33. Hsu, H.-Y.; Ji, L.; Du, M.; Zhao, J.; Yu, E. T.; Bard, A. J. Optimization of PbI_2/$MAPbI_3$ Perovskite Composites by Scanning Electrochemical Microscopy. *J. Phys. Chem. C* **2016,** *120,* 19890-19895. DOI: 10.1021/acs.jpcc.6b07850
34. Shinde, P.; Peng, X.; Wang, J.; Ma, Y.; McNamara, L.; Hammer, N.; Gupta, A.; Pan, S. Rapid Screening of Photoanode Materials Using Scanning Photoelectrochemical Microscopy Technique and Formation of Z-Scheme Solar Water Splitting System by Coupling p- and n-type Heterojunction Photoelectrodes. *ACS Appl. Energy Mater.* **2018**, *1*, 2283-2294. DOI: 10.1021/acsaem.8b00381

35. Simpson, B. H.; Rodríguez-López, J. Electrochemical Imaging and Redox Interrogation of Surface Defects on Operating $SrTiO_3$ Photoelectrodes. *J. Am. Chem. Soc.* **2015**, *137*, 14865-14868. DOI: 10.1021/jacs.5b10256.
36. Plaza, M.; Huang, X.; Ko, J. Y. P.; Shen, M.; Simpson, B. H.; Rodríguez-López, J.; Ritzert, N. L.; Letchworth-Weaver, K.; Gunceler, D.; Schlom, D. G.; Arias, T. A.; Brock, J. D.; Abruña, H. D. Structure of the Photo-Catalytically Active Surface of $SrTiO_3$. *J. Am. Chem. Soc*. **2016**, *138*, 7816-7819. DOI: 10.1021/jacs.6b03338.
37. (a) Kosaka, T.; Teduka, Y.; Ogura, T.; Zhou, Y.; Hisatomi, T.; Nishiyama, H.; Domen, K.; Takahashi, Y.; Onishi, H.Transient Kinetics of O_2 Evolution in Photocatalytic Water-Splitting Reaction. *ACS Catal*. **2020**, *10*, 13159-13164. DOI: 10.1021/acscatal.0c04115
(b) Kosaka, T.; Ando, T.; Hisatomi, T.; Nishiyama, H.; Zhou, Y.; Domen, K.; Takahashi, Y.; Onishi, H. Microelectrode-Based Transient Amperometry of O_2 Adsorption and Desorption on a $SrTiO_3$ Photocatalyst Excited under Water. *Phys. Chem. Chem. Phys.* **2021**, *23*, 19386-19393. DOI: 10.1039/D1CP03264J
38. Zhao, F.; Plumeré, N.; Nowaczyk, M. M.; Ruff, A.; Schuhmann, W.; Conzuelo, F. Interrogation of a PS1-Based Photocathode by Means of Scanning Photoelectrochemical Microscopy. *Small* **2017**, *13*, 1-8. DOI: 10.1002/smll.201604093
39. (a) Bae, J. H.; Nepomnyashchii, A. B.; Wang, X.; Potapenko, D. V.; Mirkin, M. V. Photo-Scanning Electrochemical Microscopy on the Nanoscale with Through-Tip Illumination. *Anal. Chem.* **2019,** *91,* 12601-12605. DOI: 10.1021/acs.analchem.9b03347
(b) Askarova, G.; Hesari, M.; Wang, C.; Mirkin, M. V. Decoupling Through-Tip Illumination from Scanning in Nanoscale Photo-SECM. *Anal. Chem.* **2022**, *94*,7169-7173. DOI: 10.1021/acs.analchem.2c00753
40. Askarova, G.; Barman, K.; Mirkin, M. V. manuscript in preparation.
41. Barman, K.; Wang, X.; Rui, J.; Mirkin, M. V. Mediated Charge Transfer at Nanoelectrodes: a New Approach to Electrochemical Reactivity Mapping and Nanosensing. *J. Am. Chem. Soc.* **2021**, *143*, 8547-8551. DOI: 10.1021/jacs.1c02532
42. Bard, A. J. Inner-Sphere Heterogeneous Electrode Reactions. Electrocatalysis and Photocatalysis: The Challenge*. J. Am. Chem. Soc.* **2010**, *132*, 7559-7567. DOI: 10.1021/ja101578m
43. Nioradze, N.; Chen, R.; Kurapati, N.; Khvataeva-Domanov, A.; Mabic, S.; Amemiya, S. Organic Contamination of Highly Oriented Pyrolytic Graphite as Studied by Scanning Electrochemical Microscopy. *Anal. Chem.* **2015**, *87*, 4836-4843. DOI: 10.1021/acs.analchem.5b00213.
44. Ham, Y.; Hisatomi, T.; Goto, Y.; Moriya, Y.; Sakata, Y.; Yamakata, A.; Kubota, J.; Domen, K. Flux-Mediated Doping of $SrTiO_3$ Photocatalysts for Efficient Overall Water Splitting*. J. Mater. Chem. A* **2016**, *4*, 3027-3033. DOI: 10.1039/C5TA04843E
45. Sun, P.; Mirkin, M. V. Kinetics of Electron Transfer Reactions at Nanoelectrodes. *Anal. Chem.* **2006**, *78*, 6526-6534. DOI: 10.1021/ac060924q.
46. Nioradze, N.; Chen, R.; Kim, J.; Shen, M.; Santhosh, P.; Amemiya, S. Origins of Nanoscale Damage to Glass-Sealed Platinum Electrodes with Submicrometer and Nanometer Size. *Anal. Chem*. **2013**, *85*, 6198-6202. DOI: 10.1021/ac401316n
47. Wang, X.; Han, L.; Xin, H.; Mirkin, M. V. TEM-Assisted Fabrication of Sub-10 nm Scanning Electrochemical Microscopy Tips. *Anal. Chem.* **2019**, *91*,15355-15359. DOI: 10.1021/acs.analchem.9b043

48. Barnes, J. T.; Griffith, K. J.; Beeler, J. A.; Gerroll, B. H.; Petro, A. G. C.; Williams, C. G.; Siedle, A. R.; Tait, S. L.; Peters, D. G. Alkyl-Group Grafting onto Glassy Carbon Cathodes by Reduction of Primary Monohaloalkanes: Electrochemistry and X-ray Photoelectron Spectroscopy Studies. *J. Electroanal. Chem.* **2020**, *856*, 113531. DOI: 10.1016/j.jelechem.2019.113531
49. Bo, T.; Wang, X.; Jia, R.; Han, L.; Xin, H. L.; Zhang, H.; Miller, E. M.; Mirkin, M. V. Probing Activities of Individual Catalytic Nanoflakes by Tunneling Mode of Scanning Electrochemical Microscopy. *J. Phys. Chem. C* **2021**, *125*, 25525-25532. DOI: 10.1021/acs.jpcc.1c07309
50. Zhao, Z.; Goncalves, R. V.; Barman, S. K.; Willard, E. J.; Byle, E.; Perry, R.; Wu, Z.; Huda, M. N.; Moulé, A. J.; Osterloh, F. E. Electronic Structure Basis for Enhanced Overall Water Splitting Photocatalysis with Aluminum Doped $SrTiO_3$ in Natural Sunlight. *Energy Environ. Sci.* **2019**, *12*, 1385–1395. DOI: 10.1039/c9ee00310j
51. Han, R.; Melo, M. A. Jr; Zhao, Z.; Wu, Z.; Osterloh, F. E. Light Intensity Dependence of Photochemical Charge Separation in the $BiVO_4$/Ru-$SrTiO_3$:Rh Direct Contact Tandem Photocatalyst for Overall Water Splitting. *J. Phys. Chem. C* **2020**, *124*, 9724-9733. DOI: 10.1021/acs.jpcc.0c00772

TOC graphic